

# Nuclear Breakup of Borromean Nuclei

G. F. Bertsch, and K. Hencken

*Institute for Nuclear Theory, University of Washington, Seattle, Washington 98195*

and H. Esbensen

*Physics Division, Argonne National Laboratory, Argonne, Illinois 60439*

## Abstract

We study the eikonal model for the nuclear-induced breakup of Borromean nuclei, using  $^{11}\text{Li}$  and  $^6\text{He}$  as examples. The full eikonal model is difficult to realize because of six-dimensional integrals, but a number of simplifying approximations are found to be accurate. The integrated diffractive and one-nucleon stripping cross sections are rather insensitive to the neutron–neutron correlation, but the two-nucleon stripping does show some dependence on the correlation. The distribution of excitation energy in the neutron–core final state in one-neutron stripping reactions is quite sensitive to the shell structure of the halo wave function. Experimental data favor models with comparable amounts of  $s$ - and  $p$ -wave in the  $^{11}\text{Li}$  halo.

## I. INTRODUCTION

Halo nuclei having a very weakly bound neutron pair (often referred to as Borromean nuclei) are interesting objects but they are difficult to study experimentally. Secondary interactions in radioactive beams have been an important tool, with Coulomb excitation providing quantitative data about the excitation properties [1,2]. Nuclear excitation is also important from an experimental point of view, but the theoretical interpretation of nuclear reaction cross sections deserves closer attention. In this work we attempt to make a link, as quantitative as possible, between the nuclear excitation observables and the fundamental properties of a Borromean nucleus. The fact that correlations can play an important role makes this goal more difficult than for a nucleus with a single-nucleon halo. On the experimental side, we have been inspired by the work on  $^{11}\text{Li}$  carried out at Ganil, NSCL, RIKEN and most recently at GSI. The extremely large Coulomb breakup cross section shows the halo character of the nucleus, but the details of its wave function have been controversial. Starting from the shell model, two of us [3] constructed a wave function that fit many Coulomb excitation measurements [4]. It had a dominant  $p_{1/2}^2$  shell configuration, as one expects from Hartree-Fock theory. However, several measurements (see for example ref. [5]) and also the spectroscopy of the nearby nucleus  $^{11}\text{Be}$  suggest a leading  $s_{1/2}^2$  configuration in  $^{11}\text{Li}$ .

In principle, a nuclear-induced breakup gives independent information, and so it is desirable to calculate the various cross sections and compare with experiment. A recent experiment [6] was carried out on a  $^{12}\text{C}$  target at 280 MeV/n. At that energy it is justified to treat the target-projectile interaction in the sudden approximation, using the NN forward scattering amplitude for the interaction. Thus we may neglect the evolution of the wave function during the interaction time, provided we take the interaction from nucleon-nucleon scattering. The energy domain around 250 MeV has an additional advantage from a theoretical point of view: the real part of the NN forward scattering amplitude goes through zero in this vicinity, so only the absorptive part of the interaction needs to be treated in the theory.

The nuclear excitation of Borromean nuclei have been considered by a number of authors [7–10,12,11,13]. In treating the differential cross sections, it common to make a number of simplifying assumptions. We list them here:

- Ground state wave function. Neutron–neutron correlations were neglected in ref. [8]. We shall apply wave functions that have the full three-particle correlations. It turns out that differential cross sections are quite insensitive to these correlations, except the two-neutron stripping which does show an effect. Independent particle models can only describe pure configurations, so a mixture of  $s$ - and  $p$ -waves requires a correlated model.
- Reaction model. In this work we use an eikonal model description of the nuclear reaction, improving on the black disk model of ref. [8].
- Neutron–core potential. It is important to include the final state neutron-core potential in calculating the energy or momentum spectra, as demonstrated in ref. [13]. Ref. [7] made use of simplified two-body wave functions which were based on a zero range neutron–core potential. We shall use a more realistic, finite range potential, both in the initial and final states.

We shall investigate the validity of these as well as other approximations that are often made. Our main interest is the sensitivity of experiments to the properties of the halo nucleus. In a previous work [14] we developed models of the  $^{11}\text{Li}$  ground state wave function with differing amounts of  $s$ -wave. One of our objectives is to see how well the amount of  $s$ -wave can be determined by the observables in a breakup reaction. The observables we consider are integrated cross sections for diffraction and one- and two-nucleon removal, and the differential cross section for the excitation energy in the  $^9\text{Li} + n$  final state when one neutron has been removed.

## II. REACTION MODEL

The sudden approximation leads to the eikonal model for nucleus-nucleus interactions. In previous studies, we have applied the model to the nuclear-induced breakup of single-nucleon halo nuclei [15]. Here we apply it to the breakup of a two-neutron halo nucleus. The effect of the interaction with the target to multiply the halo wave function by the profile functions  $S(R_i)$  for each particle, where  $R_i$  denotes the impact parameter of particle

$i$  with respect to a target nucleus. The halo nucleus  $^{11}\text{Li}$  has two neutrons and a  $^9\text{Li}$  core, requiring two types profile functions,  $S_n$  and  $S_c$ , associated with a neutron and the core, respectively. There are three integrated cross sections that leave the core intact, namely the diffractive, the one-nucleon stripping, and the two-nucleon stripping cross sections. These can be written

$$\sigma_{dif} = \int d^2 R_{cm} \left[ \langle (1 - S_c(R_c) S_n(R_1) S_n(R_2))^2 \rangle - \langle (1 - S_c(R_c) S_n(R_1) S_n(R_2)) \rangle^2 \right] \quad (1a)$$

$$= \int d^2 R_{cm} \left[ \langle S_c^2(R_c) S_n^2(R_1) S_n^2(R_2) \rangle - \langle S_c(R_c) S_n(R_1) S_n(R_2) \rangle^2 \right], \quad (1b)$$

$$\sigma_{1n-st} = 2 \int d^2 R_{cm} \langle S_c^2(R_c) S_n^2(R_2) (1 - S_n^2(R_1)) \rangle, \quad (2)$$

$$\sigma_{2n-st} = \int d^2 R_{cm} \langle S_c^2(R_c) (1 - S_n^2(R_1)) (1 - S_n^2(R_2)) \rangle, \quad (3)$$

where  $R_{cm}$  is the impact parameter of the halo nucleus with respect to the target nucleus, and  $\langle \dots \rangle$  denotes a ground state expectation value. Our ground state wave function  $\Psi_0$  is expressed in terms of the relative neutron-core distances,  $r_1$  and  $r_2$ . An example of the needed expectation values is the one-nucleon stripping integral

$$\langle S_c^2 S_n^2 (1 - S_n^2) \rangle = \int d^3 r_1 d^3 r_2 |\Psi_0(r_1, r_2)|^2 S_c^2(R_c) S_n^2(R_c + r_{2\perp}) (1 - S_n^2(R_c + r_{1\perp})). \quad (4)$$

The integrations are here performed for fixed  $R_{cm}$  so one should use  $R_c = R_{cm} - (r_{1\perp} + r_{2\perp}) / (A_c + 2)$ , where  $A_c$  is the mass number of the core nucleus.

The six-dimensional integration in eq. (4) is very time consuming to carry out unless some simplification are made in the wave function or in the profile functions. We shall consider two simplifying approximations. The first is the *no-recoil limit* in which the impact parameter of the core,  $R_c$ , is assumed to coincide with the impact parameter  $R_{cm}$  of the halo nucleus. The core profile function  $S_c$  can then be taken outside the expectation value. In addition, the integrations over  $r_1$  and  $r_2$  become independent and the six-dimensional integral separates into a product of two three-dimensional integrals.<sup>1</sup> Another simplifying approximation is the *transparent limit*, defined here by setting the factor  $S_n^2(R_2)$  equal to one inside the expectation value of eq. (2), thus neglecting the absorption of the second neutron. These two assumptions yield the cross section

$$\sigma_{1n-st,trans} = 2 \int d^2 R S_c^2(R) \langle 1 - S_n^2(R + r_{1\perp}) \rangle. \quad (5)$$

Note that this cross section is identical to the sum of the one- and two times the two-neutron stripping cross section,

$$\sigma_{1n-st,trans} = \sigma_{1n-st} + 2\sigma_{2n-st}. \quad (6)$$

---

<sup>1</sup>As discussed later on, the no-recoil limit differs from the exact calculation only in the case of diffraction.

We will see later that the two-neutron stripping cross section is rather small, so the transparent limit is a good approximation for this cross section.

Of course, much more information about the halo is contained in differential final state distributions. The diffractive cross section has three particles in the final state, but that distribution is beyond what we can calculate, requiring three-particle continuum wave functions for many partial waves. The one-neutron stripping leaves two particles in the final state, and the differential cross section for that state is amenable to computation. The expression for the momentum distribution associated with the relative motion of the two surviving particles is

$$\frac{d\sigma_{st}}{d^3k} = 2 \int d^2R_1 [1 - S_n^2(R_1)] \int d^3r_{2c} |M(R_1, r_{2c}, k)|^2, \quad (7)$$

where  $r_{2c}$  is the center-of-mass coordinate of the remaining neutron–core system with respect to the stripped neutron; the associated impact parameter with respect to the target nucleus is denoted by  $R_{2c}$ ,  $R_{2c} = R_1 + r_{2c\perp}$ . The amplitude  $M$  is given by

$$M = \int d^3r_2 \psi_c^*(k, r_2) S_c(R_c) S_n(R_2) \Psi_0(r_1, r_2). \quad (8)$$

Here  $\psi_c(k, r_2)$  is the continuum wave function of the surviving neutron–core system, normalized to a plane wave at infinity. The coordinates  $R_c$ ,  $R_2$  and  $r_1$  are expressed in terms of the integration variables as  $R_c = R_{2c} - r_{2\perp}/(A_c + 1)$ ,  $R_2 = R_{2c} + r_{2\perp}A_c/(A_c + 1)$ , and  $r_1 = -r_{2c} + r_2/(A_c + 1)$ .

The numerical calculation of eq. (8) is rather difficult because of the form of the ground state wave function that we apply (see the next section). A major simplification is achieved by adopting the approximation  $r_1 = -r_{2c}$  in the ground state wave function. The amplitude is then given by

$$M' = \int d^3r_2 \psi_c^*(k, r_2) S_c(R_c) S_n(R_2) \Psi_0(-r_{2c}, r_2). \quad (9)$$

An even simpler approximation is to also ignore the recoil correction in the argument of the core profile function, i. e. setting  $R_c = R_{2c}$ , and to use the transparent limit for the second neutron, i. e. setting  $S_n(R_2) = 1$ . We shall refer to these approximations as the *no-recoil*, *transparent limit*, where the amplitude reduces to

$$M'' = S_c(R_{2c}) \int d^3r_2 \psi_c^*(k, r_2) \Psi_0(-r_{2c}, r_2). \quad (10)$$

This approximation is used in ref. [9] and [13]. We will discuss the validity of the various approximations in Sec. VII below.

### III. THE THREE-BODY WAVE FUNCTION

In ref. [14] we constructed several three-body models of  $^{11}\text{Li}$ . The models are based on Hamiltonians that all reproduce the empirical neutron–neutron scattering length and all have a binding energy of the three-body system close to the empirical value of  $295 \pm 35$

keV [16]. The single-particle potentials and the density-dependence of the neutron–neutron interaction are varied to produce different probabilities of  $s$ - and  $p$ -waves in the different models. We will specifically examine the observables for models having 4.5%, 23%, and 50%  $s$ -wave. The first model is similar to the one used in ref. [3]. The second and third models are constructed with a deeper neutron–core potential for even parity, single-particle states to increase the  $s$ -wave component in the ground wave function. Details of the procedure and the first two models are given in ref. [14]. The wave functions are calculated in the form of single-particle states  $u(r)$  and amplitudes  $\alpha$  as

$$\psi_0(\vec{r}_1, \vec{r}_2) = \sum_{lj} \sum_{n,n'} \alpha_{ljnn'} u_{ljn}(r_1) u_{ljn'}(r_2) [(ls)^j (ls)^j]^0 \quad (11)$$

where  $\vec{r}_1$  and  $\vec{r}_2$  are neutron–core separation vectors. The indices  $(ls)^j$  label the single-particle, spin-angle wave functions which are coupled to zero total angular momentum as indicated by the superscript on the bracket. The indices  $n, n'$  label the radial quantum numbers of the single-particle basis states. These states are discretized by putting the system into a spherical box of large radius (typically 40 fm).

In Table I we give some characteristics of the Hamiltonians and the resulting ground state wave-functions. A useful quantity is the  $s$ -wave scattering length. Within the constraints of our three-body model, we can only produce wave functions that are predominantly  $s$ -wave by using neutron–core potentials that produce extremely large  $s$ -wave scattering lengths. The parameters of the potential for the odd-parity states are fixed by the position of the  $p_{1/2}$  resonance, which we assume to be at  $E_r = 540$  keV as suggested by measurements [17]. Besides the  $s$ -wave probability, these wave functions show significant differences. The single-particle densities of the three models are shown in Fig. 1. It may be seen that the halo is more extended the larger the  $s$ -wave probability. This is also apparent from the mean square neutron radii computed in Table I.

The integrated dipole strength for Coulomb breakup is proportional to the mean square radius of the two-neutron center of mass, given in the last column of Table I. The value obtained with the p89 wave function is consistent with the experimental Coulomb breakup, but the s50 value is much too high. Thus, we cannot regard that wave function as realistic.

Another important property of the wave function is the correlation between the two neutrons. The integrated dipole strength is proportional to the dineutron–core mean square radius, which in turn depends on the matrix element of  $\vec{r}_1 \cdot \vec{r}_2$ , as shown in [3]. In that work it was found that the correlation increased the dipole strength by 43 %. This enhancement does not depend very much on the model; with the present wave functions it is in the range of 30-40%, which may be extracted from the mean square radii computed in Table I.

We also constructed  $s$ - and  $p$ -wave independent-particle models for comparison purposes. In these models, the single-particle potential is adjusted to match the exponential fall-off of the single-particle density that is obtained with the three-body model s23 mentioned in Table I. We see from Fig. 1 that the pure  $s$ -wave model gives a much more diffuse halo than the  $p$ -wave model or the correlated models.

#### IV. PROFILE FUNCTIONS

We now specify the profile functions  $S_n$  and  $S_c$  that we use for our cross section calculations. The neutron profile function  $S_n$  in the eikonal approximation is expressed in terms of the density of the target  $\rho_t$  and the nucleon-nucleon cross section  $\sigma_{nn}$  as

$$S(b) = \exp\left[-\frac{\sigma_{nn}}{2} \int dz \rho_t(\sqrt{b^2 + z^2})\right]. \quad (12)$$

We model the density of the  $^{12}\text{C}$  target with the harmonic oscillator fit to the charge density of ref. [18],

$$\rho(r) = \rho_0 [1 + \alpha(r/a)^2] e^{-(r/a)^2}, \quad (13)$$

with  $a = 1.687$  fm and  $\alpha = 1.067$ . The nucleon-nucleon cross section is taken from ref. [19]; it is 29.2 mb at 280 MeV beam energy.

The reliability of the model can be checked against the nucleon-carbon cross sections. The predicted reaction and elastic cross sections in the eikonal model are

$$\sigma_{re} = \int d^2b [1 - S_n^2(b)], \quad (14)$$

$$\sigma_{el} = \int d^2b [1 - S_n(b)]^2. \quad (15)$$

These are compared with experiment in Fig. 2. The nucleon-carbon reaction cross section is taken from the proton cross section data tabulated in ref. [20], quoting ref. [21]. The total cross section for nucleon-carbon scattering is taken from the neutron measurements of ref. [22]. The experimental elastic cross section is deduced from the difference between total and reaction cross section. The agreement between our parameterization of  $S_n$  and experiment is close enough that we will not attempt to adjust the profile function to make a better fit. In the next section we will discuss how the cross sections in halo nuclei depend on the nucleon-target cross sections.

The core-target profile function requires the convolution of both densities,

$$S_c(b) = \exp\left[-\frac{\sigma_{nn}}{2} \int dx dy \int dz \rho_c(\sqrt{(x-b)^2 + y^2 + z^2}) \int dz' \rho_t(\sqrt{x^2 + y^2 + z'^2})\right].$$

For the density of  $^9\text{Li}$ , we note that it has the same number of neutrons as  $^{12}\text{C}$  and we will accordingly take the same parameters for the neutrons. The proton density does not have as many particles in the  $p$  shell, and we apply the pure harmonic oscillator model to determine  $\alpha$  ( $= 1/3$ ), and keep  $a$  the same as in  $^{12}\text{C}$ . The resulting  $^9\text{Li}$  density is parameterized as in eq. (13) with  $a = 1.687$  and  $\alpha = 0.726$ . This model gives an rms charge radius of 2.28 fm, slightly smaller than the empirical charge radius of  $^7\text{Li}$  which is 2.39 fm. However, the predicted cross section at 800 MeV/n is 840 mb (assuming  $\sigma_{nn} = 40$  mb), just 5% larger than the measured cross section of  $796 \pm 6$  mb from ref. [23]. The cross section at 280 MeV/n has been measured for the mirror nucleus  $^9\text{C}$  by Blank et al. [24]. They find a cross section of  $812 \pm 34$  mb to be compared with 796 mb obtained by our model.

For the  ${}^4\text{He}$  core of  ${}^6\text{He}$  we use a 3-parameter-Fermi density function [18],

$$\rho_c(r) = (1 + wr^2/c^2) / [1 + \exp((r - c)/z)],$$

with  $w = 0.517$ ,  $c = 0.964$  fm, and  $z = 0.322$  fm. At 800 MeV/n we find a total cross section of 546 mb (486 at 280 MeV/n) again comparable with the experimental result of  $503 \pm 5$  mb [25].

## V. INTEGRATED CROSS SECTIONS

In this section we examine the integrated cross sections and compare with experimental data. It is important to understand the dependence of the cross sections on the interaction and on the properties of the halo, and to this end we first discuss some estimates and bounds on the cross sections.

### A. Cross section bounds

Let us first consider the (unrealistic) limit where the core-target interaction is ignored<sup>2</sup>. For a single-nucleon halo the stripping cross section would then be identical to the reaction cross section  $\sigma_{re}$  between the nucleon and the target. In the case of a two-nucleon halo, the stripping cross section is just doubled. Split into 1n- and 2n-stripping components, the relation is

$$\sigma_{1n-st}^0 + 2\sigma_{2n-st}^0 = 2\sigma_{re}. \quad (16)$$

The symbol  $\sigma^0$  is a reminder that the core shadowing is neglected, i.e. the factor  $S_c$  is set equal to one. Eq. (16) is illustrated in Fig. 3, showing the comparison of the left- and right-hand sides of the equation for the case of  ${}^{11}\text{Li}$  breakup on a  ${}^{12}\text{C}$  target. We used the s23 model to evaluate the unshadowed cross section. The relative amounts of 1n- and 2n-stripping depends of course on the wave function and details of the interaction; in the case considered here, the 1n-stripping cross section is an order of magnitude larger than the 2n stripping.

The diffraction cross section is much more difficult to bound or estimate without full calculation of the integrals. In the case of a one-nucleon halo, a bound can be obtained by dropping the second term in the equation analogous to eq. (1a). The first term is just the elastic nucleon-target cross section, so the bound is  $\sigma_{dif}^0 \leq \sigma_{el}$ . For  ${}^{11}\text{Be}$  at 800 MeV/n and using the model of [15] we get  $\sigma_{dif}^0 = 68$  mb, smaller than the bound  $\sigma_{el} = 85$  mb. This shows that the neglected term is not necessarily small. For the two-nucleon diffraction formula eq. (1a) the first term does not reduce to the elastic scattering, so no strict bound can be obtained this way.

---

<sup>2</sup>This is commonly referred to as the transparent limit but we have reserved that concept for the transparency of the second neutron in a 1n-stripping reaction, c. f. Sec. II.

Instead, we shall analyze diffractive cross section qualitatively using a grey-disk model for the nucleon-target interaction. Thus, we take the nucleon profile function to be of the form  $S_n(b) = 1 - t\theta(b_0 - b)$ ,  $0 \leq t \leq 1$ . We also need to assume that the two nucleons are uncorrelated in the halo wave function. The diffraction cross section may then be expressed as

$$\sigma_{dif}^0 = 2\sigma_{el} \left[ 1 - (1 + 2t - t^2/2)a\langle\rho_t\rangle + 2ta^2\langle\rho_t^2\rangle - \frac{t^2}{2}a^3\langle\rho_t^3\rangle \right], \quad (17)$$

where  $\langle\rho_t^n\rangle$  is the  $n$ -th moment of the transverse nucleon density in the halo<sup>3</sup> and  $a = \pi b_0^2$ . The leading term is twice the nucleon-target elastic cross section and the corrections are controlled by the parameter  $a\langle\rho_t\rangle$ . The coefficient of the first correction is negative, so the first term gives a bound that is valid for large halos and small targets,

$$\sigma_{dif}^0 \leq 2\sigma_{el}. \quad (18)$$

In the case of a  $^{12}\text{C}$  target, the experimental elastic and reaction cross sections may be fit with  $a = 30 \text{ fm}^2$  and  $t = 0.5$ . The transverse halo density for the  $^{11}\text{Li}$  wave functions has the order of magnitude  $\langle\rho_t\rangle \approx 1/100 \text{ fm}^{-2}$  and the second term makes about a factor of two correction; the higher terms are less important. The actual numbers for our model of the  $^{11}\text{Li}-^{12}\text{C}$  reaction are shown in Fig. 3. We find  $\sigma_{dif}^0 = 75 \text{ mb}$ , reduced from  $2\sigma_{el}$  by about a factor  $2/3$ , as expected from the above analysis.

## B. Core shadowing

In this section we examine the effect of the core shadowing on the cross sections, and use again the model s23 for the ground state wave function. Fig. 3 shows on the right the shadowing effect of the carbon target in the  $^{11}\text{Li}$  breakup reaction. The 1n-stripping cross section is reduced to 43% of the unshadowed value  $\sigma_{1n-st}^0$ . The shadowing factor for the diffractive cross section is very similar (44%) to that for the 1n-stripping.

The shadowing factor for two-nucleon stripping is much stronger than for the other processes; it reduces the cross section to 20% of the unshadowed value. The difference may be understood qualitatively as follows. The one-nucleon stripping and the diffractive excitation require avoiding an absorptive interaction with a least one of the halo nucleons, favoring moderately large impact parameters. On the other hand, the two-nucleon absorption has no such restriction and would be concentrated entirely at small impact parameters but for the presence of  $S_c$ . The different dependences on impact parameter is shown in Fig. 4. Here we see that the 2n-stripping probability is more concentrated at small impact parameter than the 1n-stripping and the diffractive probabilities, which are very similar to each other.

The shadowing factor varies, of course, with target size. This dependence is illustrated in Fig. 5, where the target densities were taken from [18,26]. We see that the shadowing changes by a factor of 2 both for diffraction and 1n-stripping, going from a  $^4\text{He}$  target to a heavy target, and by a factor of 4 for the 2n-stripping.

---

<sup>3</sup>More precisely, it is the  $n$ -th moment of an averaged transverse density, the averaging being over the shape of the nucleon profile function.

### C. Wave function sensitivity

We next consider the sensitivity of the cross sections to properties of the halo wave functions. The various cross sections for different models are given in Table II. For the single-nucleon stripping cross section, the shadowing factor varies, depending on how extended the single-particle density is. From Table I, we see that the mean square radius of the halo increases as the  $s$ -wave probability increases. Thus we expect less shadowing and a larger cross section for the models with a larger  $s$ -wave. This is indeed born out by the numbers in Table II. For the two-nucleon stripping, the correlation between the neutrons should be important as well, as they must both interact with the target. Indeed, we see from Table II that the two-nucleon cross sections doubles going from an uncorrelated  $p$ -wave model to the model with correlations and  $p$ -wave dominance. This may be compared with the effect of the correlations on the dipole transition strength which, as was mentioned in the last section, gives only a 30-40% enhancement.

### D. ${}^6\text{He}$ cross sections

Here we report corresponding cross sections for the breakup of  ${}^6\text{He}$  on a  ${}^{12}\text{C}$  target, using the  ${}^6\text{He}$  wave function from ref. [14], line 5 of Table II. The cross sections for two different beam energies are shown in Table III.  ${}^6\text{He}$  is more tightly bound than  ${}^{11}\text{Li}$ , so the halo density does not extend out as far. Another difference is that  ${}^6\text{He}$  has a dominant  $p_{3/2}$  shell configuration which allows a stronger spatial correlation; pure  $s_{1/2}$  or pure  $p_{1/2}$  configurations, on the other hand, have uncorrelated densities. The larger correlation implies that the 2n-stripping will be relatively stronger. This is indeed seen to be the case in Table III; the 2n-stripping cross sections is about a factor of two larger for  ${}^6\text{He}$  than for  ${}^{11}\text{Li}$ . Otherwise, the cross sections are about the same as for  ${}^{11}\text{Li}$ . The shadowing factors are similar, due to balancing features of a smaller core and a less extended halo.

## VI. SHAPE OF THE STRIPPING SPECTRUM

In this section we discuss analytic forms for the shape of the spectrum in the neutron-core system produced by the 1n-stripping reaction. The standard parameterization of a peaked distribution by the Breit-Wigner function is not justified at energies close to zero, or for the overlaps with extended wave functions. We shall propose parameterizations that take into account the threshold behavior and the halo character of the initial state. Throughout this section we make use of the no-recoil, transparent limit defined in eq. (10).

To treat the one-neutron removal from a Borromean nucleus, we simply take the overlap of the initial ground state wave-function with the continuum final state of the neutron-core system (cf. eq. (10)), fixing the position  $r_1 = -r_{2c}$  of the stripped neutron. The stripping model assumes that the process is incoherent in  $r_1$ . Thus we consider matrix elements of the form

$$M''(r_1, k) = \int d^3r_2 \psi_k^*(r_2) \psi_0(r_1, r_2) \quad (19)$$

and a probability distribution of the form

$$|M''(r_1, k)|^2 dn_k.$$

Here  $dn_k \sim k^2 dk$  for a differential momentum distribution and  $dn_k \sim kdE$  for a differential distribution in excitation energy of the neutron–core system.

Different partial waves of the continuum wave function are incoherent if we integrate over the direction of the decay distribution. At low energies the  $s$ - and  $p$ - waves will be most important, and we now discuss their functional behavior.

### A. $s$ -Wave distribution

The  $s$ -wave distribution can be described analytically in the limit where the wave functions are dominated by their asymptotic behavior<sup>4</sup>. The continuum  $s$ -wave is then given by

$$\psi_0 \sim \frac{\sin(kr + \delta)}{kr}.$$

Here  $\delta$  is the  $s$ -wave phase shift; the scattering length is the linear coefficient in the expansion

$$\delta = -ak + O(k^3).$$

The two-particle initial state wave function has no exact analytic limit, but the general exponential fall-off at large distances suggests the approximation

$$\psi(r_2, r) \approx f(r_2) \frac{e^{-\alpha r}}{r}.$$

Then the integral in eq. (19) can be carried out to give

$$M'' \sim \frac{\cos(ka) - \alpha/k \sin(ka)}{k^2 + \alpha^2},$$

and therefore the cross section for the  $s$ -wave is given by

$$\frac{d\sigma}{dE} \sim k \left[ \frac{1}{\alpha^2 + k^2} \right]^2 \left[ \cos(ka) - \frac{\alpha}{k} \sin(ka) \right]^2. \quad (20)$$

This depends on the initial state potential through the fall-off parameter  $\alpha$  and on the final state potential through the scattering length  $a$ . If the two potentials are the same, then the orthogonality of initial and final states requires the matrix element to vanish. This comes about in eq. (20) to leading order in  $k$  by the well-known relation between binding energy and scattering length [28].

---

<sup>4</sup>The formula derived gives an excellent description of the magnetic photo-disintegration of the deuteron at low energy [27].

The  $s$ -wave energy distribution for  $^{11}\text{Li}$  is shown in Fig. 6. Here we have fitted both parameters  $\alpha$  and  $a$  to give the best agreement with the calculated curve, which was obtained in the no-recoil, transparent limit (cf. eq. 10) using the model s23. In principal  $\alpha$  is given by the binding energy as  $\alpha \approx \sqrt{2mE_B}$ . Our fit has  $\alpha = 24.5$  MeV/c. The corresponding binding energy is 0.32 MeV, almost equal to the binding energy of the independent particle model. Also our fitted value  $a = -4.7$  fm is very close to the actual scattering length of  $-5.6$  fm.

The distribution in Fig. 6 peaks at very low energies; the peak position is close to the momentum  $k = \alpha/2$  for a fairly wide range of scattering lengths  $a$  between  $-1/\alpha < a < 1/\alpha$ . This corresponds to an energy peak  $E_{peak}$  at

$$E_{peak} = E_B/4.$$

With our theoretical fit,  $E_{peak} \approx 0.08$  MeV. It should also be mentioned that for models with very large scattering lengths, such as the s50 model, the scattering length sets the momentum scale and the predicted peak is lower in energy.

The corresponding  $s$ -wave distribution for  $^6\text{He}$  is shown in Fig. 7. Here the best scattering length parameters is  $a = 1.6$  fm, to be compared with the actual scattering length of  $a = 2.4$  fm associated with the  $^5\text{He}$  potential. The best fit value of  $\alpha$  is  $\alpha = 55$  MeV/c; this may be compared with the binding energy estimate  $\sqrt{2mE_B} = 43$  MeV/c.

## B. $p$ -Wave distribution

For the  $p$ -wave, measurements of the  $^{11}\text{B}(^7\text{Li}, ^8\text{B})^{10}\text{Li}$  reaction have suggested the existence of a resonance at about 540 keV [17]. In our recent study of the  $^{11}\text{Li}$  wave function we used this data to fix the  $p$ -wave potential for the neutron-core system. In this section we wish to establish a simple function to represent the distributions that we calculate. After trying different functional forms, we found that one could get acceptable fits with the Breit-Wigner resonance form but using an energy-dependent width. The threshold behavior of a  $p$ -wave resonance requires a width depending on energy as  $\Gamma \sim E^{3/2}$ . However, the width cannot continue to grow as the  $3/2$  power at energies above the resonance. We shall account for this by using the form of the  $p$ -wave width obtained in potential scattering [29]

$$\Gamma = \left(\frac{E}{E_R}\right)^{3/2} \frac{\Gamma_0}{1 + cE/E_R}. \quad (21)$$

The Breit-Wigner function for the decay of a resonance is then given by

$$\frac{d\sigma}{dE} = A \frac{\Gamma}{(E - E_R)^2 + \Gamma^2/4}. \quad (22)$$

There are four parameters here, namely the resonance energy  $E_R$ , the width on resonance  $\Gamma_0$ , the overall strength  $A$ , and a cutoff parameter  $c$ . One might think that  $\Gamma_0$  and  $c$  could be determined by the radius of the potential forming the resonance, but the fact that we are considering a transition from a halo state implies that the length scales are larger than the nuclear radius. We shall treat them as adjustable parameters. Fig. 6 shows a fit

with parameter values  $\Gamma_0 = 1$  MeV,  $E_R = 0.51$  MeV, and  $c = 1.7$ . When we make an unconstrained fit, the parameters  $\Gamma_0$  and  $c$  acquire large values, showing that the function  $\Gamma$  is close to the  $E^{1/2}$  dependence, except at extremely low energies. The deviation from the  $3/2$  power law is quite understandable; although the single-particle wave function is in a  $p$ -wave, the fact that the initial state is a halo means that the extension of the wave function rather than the radius of the barrier sets the scale for the threshold region.

In Fig. 7 we show similar a comparison for  ${}^6\text{He}$  stripping. In this case, the peak of the  $p$ -wave distribution is located at 0.83 MeV which corresponds quite well to the resonance energy of the  $p_{3/2}$  scattering state (0.89 MeV). Nevertheless, the best fit again favors large values of  $c$ , indicating that the  $3/2$  power law for the width is only valid very close to the threshold.

## VII. STRIPPING DISTRIBUTIONS

In this section we treat the full stripping cross section as defined by eqs. (7) and (9). There are a number of questions one can ask: i) How reliable is the transparent limit to deduce the shape of the differential cross section? Do we get the right shape for the  $s$  and  $p$ -wave and also the right ratio between them? ii) Can a decomposition of the differential cross section into  $s$ - and  $p$ -wave components be used to infer the  $s/p$  ratio in the ground state wave function?

The energy distribution for the full calculation is compared in Fig. 8 to the no-recoil, transparent limit for  ${}^{11}\text{Li}$  stripping, using the s23 ground state wave function. We see that the effect of the neutron shadowing is to reduce the cross section without affecting the energy distribution. Thus we can use the transparent limit with confidence in describing these distributions.

The 1n-stripping calculation involves integrations of the probability over the impact parameters of the absorbed neutron and the center of mass of the second neutron with respect to the core. These integrals are incoherent, and can be performed on a coarser mesh than the wave function integral over the internal coordinate. It is of interest to see how much the shape depends on the impact parameters, to make this integration as coarse as possible. Fig. 9 shows the distribution with the s23 wave function, comparing the full calculation with the distributions at typical impact parameters. Here we fix the value of the transverse radii  $R_{2c}$  and  $R_1$  and integrate over the angle between them, and also over the longitudinal component of  $r_{2c}$ . The curves have been normalized to the same area. We see that the ratio of cross sections at low energy to that at the  $p$ -wave peak varies by the order of 20%. Thus the impact parameter integration mesh cannot be coarser than 1 fm or so.

Next we consider the relation of the  $s$ - and  $p$ -wave probabilities in the wave function to the corresponding probabilities in the stripping distributions. In principle, the stripping distributions for  $s$ - and  $p$ -waves are sufficiently dissimilar that one should be able to extract their relative probabilities from the data. In Fig. 10 we show the percentage of these waves as would be found in the energy distributions for the full calculation and also in the no-recoil, transparent limit, using the s23 wave function. As found before, the transparent limit is very accurate for purposes of extracting these ratios. As could be anticipated from Fig. 9, it is necessary to do a complete integration over all impact parameters to determine the

theoretical ratios. Finally, the amount of  $s$ -wave in the final state stripping distribution is systematically larger than in the initial ground state wave function. This is due to the larger extension of the  $s$ -wave, and the resulting decreased shadowing by the core. In Fig. 11 we compare the  $s$ - and  $p$ -wave probabilities of the three correlated models with the final state probabilities for 1n-stripping. In all cases the  $s$ -wave probability is somewhat larger in the final state than in the wave function, for the reason given above.

## VIII. THE NO-RECOIL APPROXIMATION

In this section we examine the no-recoil approximation, and will find that it is very accurate for the  $^{11}\text{Li}$  reaction. The no-recoil approximation is in fact exact for the integrated stripping reactions, because the outer integration over  $R_{cm}$  can be changed to an integration over the core coordinate by a simple change of variable. This separation cannot be made for the diffractive cross section, so there will be some effect of including core recoil. We discuss it immediately below. Following that, we discuss the energy distribution of the single-particle stripping, which is also subject to recoil corrections.

### A. Diffraction

Diffraction arises from the fluctuations in the expectations of powers of the profile operators (see eq. (1b)), and will only be significant at impact parameters where the operators vary. There are two effects that make the diffractive scattering dependent on the distinction between the center-of-mass coordinate and the core coordinate. The first is that there are no fluctuations associated with the core profile function in the no-recoil limit, and including those fluctuations might be expected to increase the diffractive cross section. However, there is another effect that goes in the opposite direction. That is that the spatial extension of the neutrons is smaller measured with respect to the center of mass than with respect to the core. One might expect a smaller fluctuation of  $S_n$  if the neutron wave functions are more confined. Another way to look at the question is with eq. (1a). The first term in this formula can be evaluated in either coordinate system. The effect of the no-recoil approximation is thus confined to the evaluation of the second term. We have evaluated the integral numerically for the uncorrelated  $p$ -wave model, and we find that the effect of recoil is to reduce the diffractive cross section by about 20%. Since the corrections are expected to scale as  $1/A$ , one should not ignore them for nuclei lighter than  $^{11}\text{Li}$ .

### B. Stripping distributions

As shown in Sec. II we include the main recoil effect (the difference in the profile functions between  $R_c$  and  $R_{2c}$ ) in our calculation. The only approximation is then to replace the position  $r_1$  of the stripped neutron by  $-r_{2c}$ , cf. eq. (9). As this neutron is absorbed, whereas the other neutron and the core must survive, the major contribution to the spectrum comes from a region where  $r_1$  is not small. Therefore we do not expect to get a big effect from this. Nevertheless, we have also calculated the exact spectrum from eq. (8) in the independent

$p$ -wave model for fixed impact parameters  $R_{2c}$  and  $R_1$ . The overall relative deviation of the two spectra is smaller than 3% with deviation near the peak being only of the order of 1/2%. The recoil effect on the spectrum therefore seems to be negligible.

## IX. COMPARISON WITH EXPERIMENT

### A. Integrated cross sections

In Table II we compare the integrated cross sections with the experimental data of ref. [6], Table 3. The yields of events having zero, one, or two neutrons in coincidence with the  ${}^9\text{Li}$  fragment give respectively the cross sections labeled 2n-stripping, 1n-stripping, and diffraction. The first thing to note in the comparison with theory is that the total two-neutron removal cross section measured, 280 mb, is much larger than the eikonal model predicts. There are also data on the two-neutron removal cross section at 800 MeV/n [30]. Applying the eikonal model<sup>5</sup> at this energy gives a cross section of 187 mb (s23 wave function), only 15% lower than the experimental value of  $220 \pm 10$  mb. At the lower energy the s23 model gives 179 mb. This is close to the theoretical value at the higher energy, which is certainly to be expected in view of the mild change in the nucleon-nucleon cross section between the two energies. The direction of the change in both the nucleon-nucleon and the eikonal removal cross section is a decrease at the lower energy. In contrast the experimental value is larger at the lower energy. The theoretical two-neutron removal cross section behaves the same way in the case of  ${}^6\text{He}$ , as may be seen in the bottom line of Table III. Here also there is fair agreement with the experimental value at the higher energy.

Let us now turn to the individual components. The diffractive and 1n-stripping cross sections are within experimental error of the most extreme wave function, s50, but the 2n-stripping cross section far exceeds any of the models. In principle, additional contributions to the cross section could come from processes outside the scope of the eikonal model. The flux that is absorbed in the eikonal can reappear, e.g. by multistep or rearrangement processes. This might first show up in cross sections that are very small in the eikonal model—such as the 2n-stripping. On the experimental side, the definition of the cross sections requires some momentum cut on the neutrons to be considered as part of the projectile fragmentation. In ref. [6], the detector acceptance allowed neutrons with transverse momenta of up to 60 MeV/c to be included; the authors also quoted cross sections assuming that 20% of all fragmentation neutrons were outside that momentum range. The deduced cross sections are given in the last column of Table III, labeled "modified data".

As may be seen from the table, adding the detector acceptance correction explains the small 2n-stripping cross section, but only at the expense of greater disagreement with theory for the other two cross sections. Thus, for the diffractive cross section, we obtain only between 33% and 51% of the experimental value. We believe that it not possible to explain this discrepancy within the framework of the eikonal model. Recall that the unshadowed diffractive cross section has a quasibound,  $\sigma_{dif}^0 < 2\sigma_{el} \approx 120$  mb, valid for very extended

---

<sup>5</sup>We note that ref. [7] obtained 241 mb, i.e., 10% higher than experiment, in their eikonal model.

halos, and the actually computed cross section is reduced from this by two factors of two. The first reduction, seen in eq. (17), is associated with the fact that the nucleon-target profile function blocks a significant fraction of the halo density. The second factor is the shadowing of the halo density by the core-target profile function. This shadowing is unavoidable and reduces the diffraction cross section by an additional factor of two.

For the 1n stripping cross section with an assumed 20% acceptance correction, the eikonal model gives— depending on the wave function— between 63% and 83% of the experimental result. The cross section increases with larger  $s$ -wave contribution in the wave function. But we believe that the model that comes closest,  $s50$ , is unrealistic on other grounds. Until the cross sections are better understood, it will not be possible to use this sensitivity to test the  $s$ -wave probability in the wave function.

## B. Relative energy spectrum

In the analysis made in [6] two Breit-Wigner resonances were fitted, at  $0.21 \pm 0.05$  and  $0.62 \pm 0.10$  MeV, and the relative amounts of  $s$ - and  $p$ -waves in the wave function were extracted. Let us see how this compares with our analysis with the calculated distributions. As discussed in Sec. VI, we find a peak for the final  $s$ -wave at a much lower energy than the experimental spectrum shows. However, the finite angular and energy resolution of the experimental detectors will inevitably smear out the distribution of the extracted relative momentum or energy, shifting the apparent peak to higher energy. This should be taken into account in comparing our spectrum with the experiments.

The authors of ref. [6] give a table of transverse momentum and longitudinal velocity resolution widths, and we have folded these widths with the theoretical spectra to compare with experiment <sup>6</sup>. The folding is done by Monte Carlo sampling. We generate events, sampling the theoretical distribution of  $E$  in the center-of-mass system of the neutron–core system, and assuming that the angular distribution is isotropic there. We add a Gaussian-distributed center of mass momentum. As we do not have any cuts in our simulation, this center of mass momentum is not important. We transform then from the projectile frame to the lab frame, determining the transverse momentum as well as the Lorentz  $\beta$  in the lab frame. To these we add random errors from a Gaussian distribution with a full width at half maximum given by Table 2 in [6]. The relative energy (eq. in (3.2) of [6]) is reconstructed using these values, which are then binned into the same energy intervals as the experiment.

Fig. 12 shows the result of this procedure for the  $s23$  model. The experimental resolution increases the position of the  $s$ -wave peak from 0.08 MeV to 0.15 MeV, which is close to the value  $0.21 \pm 0.05$  deduced by the Breit-Wigner fit. However, with our shapes for the individual components, the measured peak at 0.21 MeV is a combined effect of both  $s$ - and  $p$ -wave. The individual spectra are strongly overlapping, and require a realistic model of the shapes to separate them with confidence.

---

<sup>6</sup> Ref. [6] also quotes an energy resolution function, ( $\Delta E \sim E^{0.75}$ ) but this does not go to a finite value near  $E = 0$ , so we prefer to construct the resolution as described.

In our treatment, there is no indication of a sharp  $p$ -wave resonance. Our shape has a long tail which explains most of the higher energy data. This fact can be demonstrated by fitting the experimental data at low energies directly to this shape. One then finds that this curve alone is capable of explaining almost all of the higher energy data, leaving no room for a resonance there.

One of our main goals is to find out what we can conclude from this spectrum about the  $s$ -wave contribution in the ground state and also about the position of the  $p$ -wave resonance. We investigate this in the following way. The shapes of the distributions are assumed to be the same as we found in Sec. VI, using the parameters of the s23 model. We allow the ratio of  $s$  to  $p$  to vary, as well as the position of the  $p$ -wave resonance (that is  $E_R$  in eq. (22)). Using this as the input to our Monte-Carlo code we calculate the simulated spectrum. Minimizing the  $\chi^2$  with the experimental result, we get the most likely result together with some range which we still consider likely. Fig. 13 shows the best fit to the experiment we get in this way. It is for an energy of  $E_R = 0.45$  MeV and an  $s$ -wave component of about 40%. From the variation of  $\chi^2$  we estimate the uncertainty in the position to be 0.1 MeV and the  $s$ -wave contribution between 30% and 50%. From Fig. 11 we estimate the  $s$ -component in the  $^{11}\text{Li}$  wave function to be between 20% and 40% and the most likely value to be about 30%.

### C. Transverse momentum distribution

In order to test our final state spectrum, we also make comparisons to a measurement of the transverse momentum distribution of neutrons. Such a measurement has recently been performed at the same energy [32]. In our analysis we assume that the momentum distribution of the neutrons is isotropic and identical to the relative momentum distribution of the neutron and the core fragment. The relative energy spectrum can then be transformed into a transverse momentum distribution:

$$\frac{d\sigma}{d^2k_{\perp}} = \int_0^{\infty} dk_l \frac{1}{2\pi mk} \frac{d\sigma}{dE}.$$

In Fig. 14 we compare the result of our “best” model with the experimental result. In this figure we made no attempt to include the experimental resolution in the theory curve. The agreement between theory and experiment is reasonable especially for medium and larger momenta, whereas we have difficulties at the very low momenta. At these momenta we expect our approximation of using the relative momenta instead of the neutron momenta to be invalid, as center of mass correction should play a role. Also in this analysis we have ignored diffraction.

## X. CONCLUSIONS AND OUTLOOK

In this paper we applied the eikonal theory to nuclear reactions of Borromean nuclei, with the object of developing a quantitative tool for interpreting reaction cross sections. Because the full theory is quite demanding from a numerical point of view, we examined the approximations that are commonly made. In particular, the theory simplifies if one neglects

correlations in the ground state wave function, the final state interaction, the distortion effects of the profile functions on unstripped particles, or the difference between vectors referred to various center-of-mass systems.

The easiest cross section to interpret is the one-particle stripping, which leaves a particle and the core in a final state of low excitation energy. The integrated one-particle stripping cross section can be calculated with rather rough approximations. The correlations in the ground state play no role except to determine occupation probabilities for the shell orbitals. In the differential cross section, the distributions of  $s$ - and  $p$ -waves are quite distinct, allowing the occupation probabilities of the  $^{11}\text{Li}$  halo orbitals to be extracted with 10-20% accuracy. Many of the simplifying approximations can be used here without significant error. The distortion introduced by the profile functions have practically no effect on the shape of the distributions, and a moderate effect on the extracted relative probabilities. However it is important to include the final state interaction in the particle-plus-core system [13]. We proposed parameterizations of the  $s$ - and  $p$ -wave distributions that take both the initial halo character and the final state interaction into account. The  $s$ -wave distribution, given by eq. (20), is derived from the asymptotic wave functions. The  $p$ -wave distribution, given by eqs. (21-22), is in the form of a Breit-Wigner function with an energy-dependent width. The width varies with energy as  $\Gamma \sim E^{3/2}$  at threshold, but the threshold region is very narrow due to the extended initial wave function. At higher energies the width grows more like  $\Gamma \sim E^{1/2}$ , which is the characteristic behavior in the absence of a barrier.

The other two integrated cross sections are more sensitive to the correlations in the wave function. The two-particle stripping cross section is sensitive to the pairing correlation, nearly doubling when pairing is included. If the two-nucleon stripping could be measured well, it could be used to study this aspect of the wave function. The other integrated cross section, the diffractive cross section, is not only sensitive to the eikonal distortions, but we found that it changes significantly if the recoil correlation is included in the wave function. The differential diffractive cross section is presently beyond our computational powers.

As a specific example, we have applied the eikonal analysis to the data of ref. [6]. The total two-neutron removal cross section is larger than our calculation, and also larger than the experimental value at a higher energy (800 MeV/n). This is surprising because the difference in nucleon-nucleon cross sections at the two energies demands the opposite trend in the eikonal model. Our calculated one-neutron stripping and diffractive cross sections are only 75% and 50% of the measured values, respectively. The experimental diffractive cross section is nearly high enough to be in conflict with the bound given by eq. (18).

In analyzing the differential cross section, we found that both  $s$  and  $p$ -waves are needed. The  $p$ -wave cross section does not give a sharp resonant peak, due to the fact that the initial wave function is largely outside the centrifugal barrier. The  $s$ -wave distribution peaks at a very low energy, and the experiment does not show as much of a threshold enhancement as we predict. While we are not able to get a perfect fit to the data, our best fit has a  $p$ -wave resonance near 0.45 MeV, only slightly lower than the measurement of ref. [17]. The peak in the stripping distribution found by [6] is at 0.2 MeV, and is most likely due to the combined effect of  $s$ - and  $p$ -waves. Again, we found that simplifying approximations of no recoil and the transparent limit give a rather good account of the one-particle stripping distribution. Our analysis with the full eikonal theory gives an  $s$ -wave component of between 30% and 50% in the cross section, which corresponds to an  $s$ -wave probability in  $^{11}\text{Li}$  between about

20% and 40%. This range also gives a good fit to the transverse momentum distribution of neutrons measured by ref. [32]. A number of other experimental [5,17,32,6,33] and theoretical studies [10,34] have extracted  $s$ -wave probabilities of about 50%. An even larger value is apparently obtained by ref. [13], who report a  $p$ -wave probability of 26%.

In conclusion, the eikonal theory has considerable promise for interpreting the distributions and cross sections in nuclear breakup, but it has not yet proved to be a quantitative tool for the reaction we studied.

## XI. ACKNOWLEDGMENT

We would like to thank W. Dostal and H. Emling for discussions and for providing unpublished data from the experiment in ref. [6]. This work was supported by the Swiss National Science Foundation (SNF), the “Freiwillige Akademische Gesellschaft” (FAG) of the University of Basel, the “Deutsche Forschungsgemeinschaft” (DFG), and the U.S. Department of Energy, Nuclear Physics Division, under Contract No. W-31-109-ENG and DE-FG-06-90ER-40561.

## REFERENCES

- [1] D. Sackett, et al., Phys. Rev. C48 (1993) 118.
- [2] S. Shimoura, et al., Phys. Lett. B348 (1995) 29.
- [3] G. F. Bertsch and H. Esbensen, Ann. Phys. **209** (1991) 327.
- [4] H. Esbensen, G.F. Bertsch, and Ieki, Phys. Rev. C48 (1993) 326.
- [5] R. A. Kryger, et al., Phys. Rev. C46 (1993) 2439.
- [6] M. Zinser, et al., Nucl. Phys. A619 (1997) 151.
- [7] Y. Ogawa, K. Yabana, and Y. Suzuki, Nucl. Phys. A543 (1992) 722.
- [8] F. Barranco, E. Vigezzi, and R.A. Broglia, Phys. Lett. 319 (1993) 387
- [9] F. Barranco, E. Vigezzi, and R.A. Broglia, Zeit. Phys. A356 (1996) 45.
- [10] I.J. Thompson and M. V. Zhukov, Phys. Rev. **C49** (1994), 1904.
- [11] Y. Ogawa, Y. Suzuki, and K. Yabana, Nucl. Phys. **A571** (1994), 784.
- [12] P. Banerjee and R. Schyam, Phys. Lett. **B349** (1995), 421.
- [13] E. Garrido, D.V. Fedorov, and A.S. Jensen, Phys. Rev. C53 (1996) 3159.
- [14] H. Esbensen, K. Hencken and G.F. Bertsch, submitted for publication, 1997.
- [15] K. Hencken, G. F. Bertsch and H. Esbensen, Phys. Rev. C54 (1996) 3043.
- [16] B. M. Young, et al., Phys. Rev. Lett. 71 (1993) 4124.
- [17] B. M. Young, et al., Phys. Rev. C49 (1994) 279.
- [18] C. DeJager, H. DeVries, and C. DeVries, At. Data and Nucl. Data Tables 17 (1974) 479.
- [19] K. Charagi and S.K. Gupta, Phys. Rev. C41 (1990) 1610.
- [20] W. Bauhoff, At. Data and Nucl. Data Tables 35 (1986) 429.
- [21] P.U. Renberg, et al., Nucl. Phys. A183 (1972) 81
- [22] J. Franz, et al., Nucl. Phys. A490 (1988) 667.
- [23] I. Tanihata, et al., Phys. Rev. Lett. 55 (1985) 2676.
- [24] B. Blank, et al., to be published (1997).
- [25] I. Tanihata, et al., Phys. Lett. 160B (1985) 380.
- [26] H. DeVries, C. DeJager and C. DeVries, At. Data and Nucl. Data Tables 36 (1987) 495.
- [27] S. deBenedetti, "Nuclear Interactions", (Wiley, N.Y., 1964), p. 274.
- [28] L. Elton, "Introductory Nuclear Theory", (Pitman, London, 1959), eq. (3.75).
- [29] A. Bohr and B. Mottelson "Nuclear Structure", Vol. I, (Benjamin, 1969), eq. (3F-38-44).
- [30] T. Kobayashi, et al., Phys. Lett. B 232 (1989) 51.
- [31] I. Tanihata, D. Hirata, T. Kobayashi, S. Shimoura, K. Sugimoto, and H. Toki, Phys. Letts B 289 (1992) 261.
- [32] M. Zinser, et al., Phys. Rev. Lett. 75 (1996) 1719.
- [33] N. Aoi et al., IV Int. Conf. on Radioactive Nucl. Beams, Omiya, Japan (June 1996).
- [34] N. Vinh Mau and J.C. Pacheco, Nucl. Phys. A607 163 (1996).

## TABLES

TABLE I. Parameter of the different models used in comparing the different cross sections. The first model (“p89”) uses the same potential for  $s$  and  $p$  wave, whereas the other two use a deeper potential for the  $s$ -wave (and all other even  $L$  waves). The strength of the  $p$ -wave potential is essentially fixed by the position of the  $p_{1/2}$  resonance. The lowest two entries give the properties of the uncorrelated pure  $s$  and  $p$ -wave models described in the text.

Model	$E_B$	$V_s$ (MeV)	$a_0$ (fm)	% $s_{1/2}$	% $p_{1/2}$	$r^2$ (fm <sup>2</sup> )	$(r_1 - r_2)^2$ (fm <sup>2</sup> )	$(\frac{r_1+r_2}{2})^2$ (fm <sup>2</sup> )
p89	-0.295	-35.4	+1.7	4.5	89.1	29.4	42.8	18.7
s23	-0.295	-47.5	-5.6	23.1	61.0	37.7	45.9	26.2
s50	-0.292	-51.5	-90.	49.9	33.9	53.8	70.1	36.2
s				100		45.0	90.0	22.5
p					100	27.5	55.0	13.8

TABLE II. Integrated cross sections (mb) with different models of the halo nucleus  $^{11}\text{Li}$ .

	uncor. s	uncor. p	p89	s23	s50	data [6]	modified data
diffraction	38	26	27	33	40	$50 \pm 10$	77
1n-stripping	174	123	121	137	162	$170 \pm 20$	195
1n-str. (transp.)	182	129	134	155	182		
2n-stripping	4	3	6	9	10	$60 \pm 20$	8
2n-removal	216	152	154	179	212	$280 \pm 30$	$280 \pm 30$

TABLE III. Integrated cross sections (mb) for  $^6\text{He}$  breakup on  $^{12}\text{C}$ . The experimental number is from ref. [31].

	240 MeV/n			800 MeV/n		
	with $S_c$	w/o $S_c$		with $S_c$	w/o $S_c$	
dif	32.3	64.5	$< 2\sigma_{el} = 119$	42.7	89.7	$< 2\sigma_{el} = 168$
1n-st	136	286		144	319	
1n-st,trans	170	409	$\approx 2\sigma_{re} = 414$	184	488	$\approx 2\sigma_{re} = 493$
2n-st	16.7	61.6		19.8	84.1	
$\sigma_{-2n}$	185			206		$\sigma_{exp} = 189 \pm 14$

FIGURES

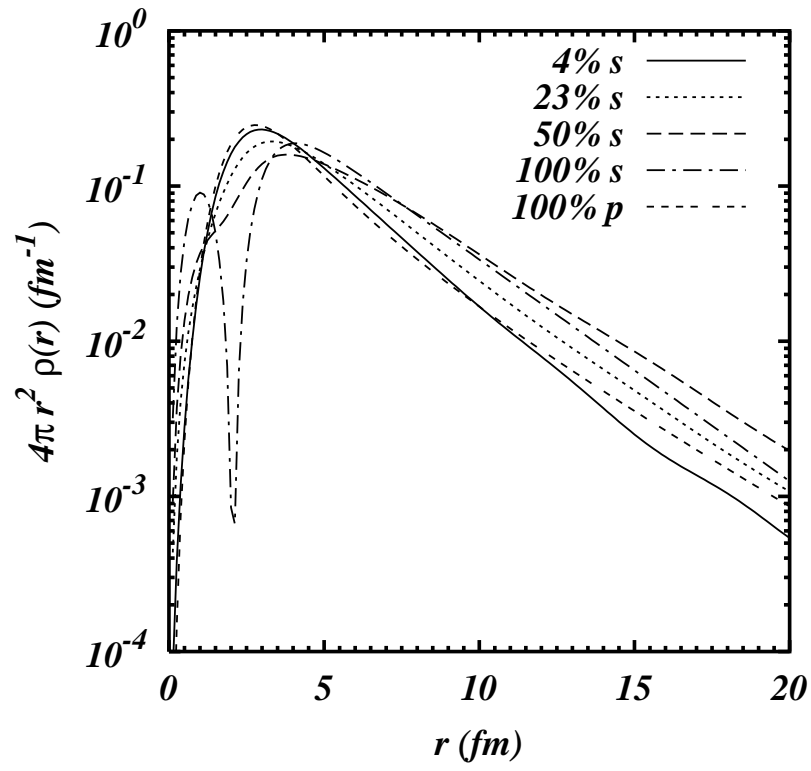


FIG. 1. Single-particle density of halo neutrons in various models of  $^{11}\text{Li}$ .

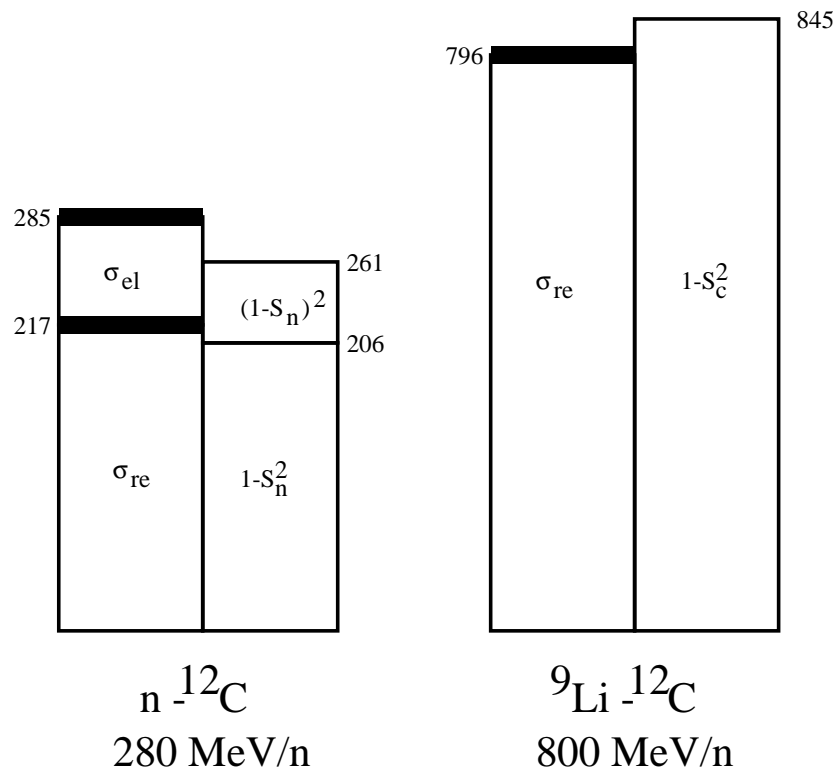


FIG. 2. Cross sections for nucleon- $^{12}\text{C}$  scattering and for  $^9\text{Li}-^{12}\text{C}$  scattering. Comparison of the results of our profile function with experimental results.

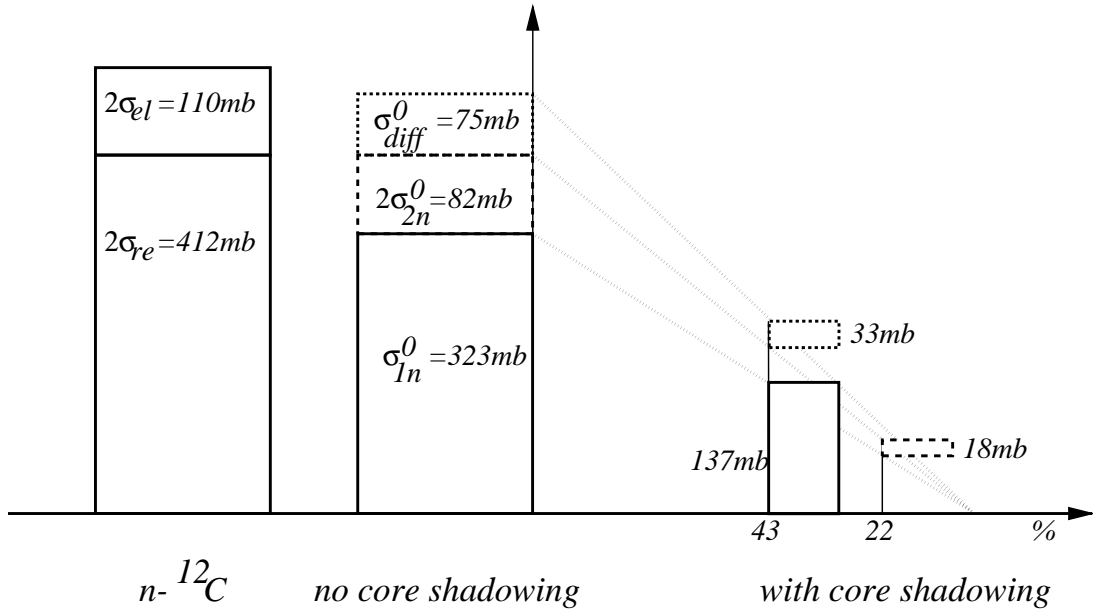


FIG. 3. Breakup reaction cross sections for  $^{11}\text{Li}\text{-}^{12}\text{C}$  scattering. The left-hand histogram shows twice the  $n\text{-}^{12}\text{C}$  cross sections as required by equality eq. (16) and the bound for the diffractive cross section, eq. (18). We compare them with the total cross sections without core shadowing (“ $\sigma^0$ ”) in the next histogram. The shadowing reduces the cross section by a factor of  $\approx 0.4$  for single-neutron stripping and diffraction, and by a factor of  $\approx 0.2$  for two-nucleon stripping, as show by the diagram on the right side.

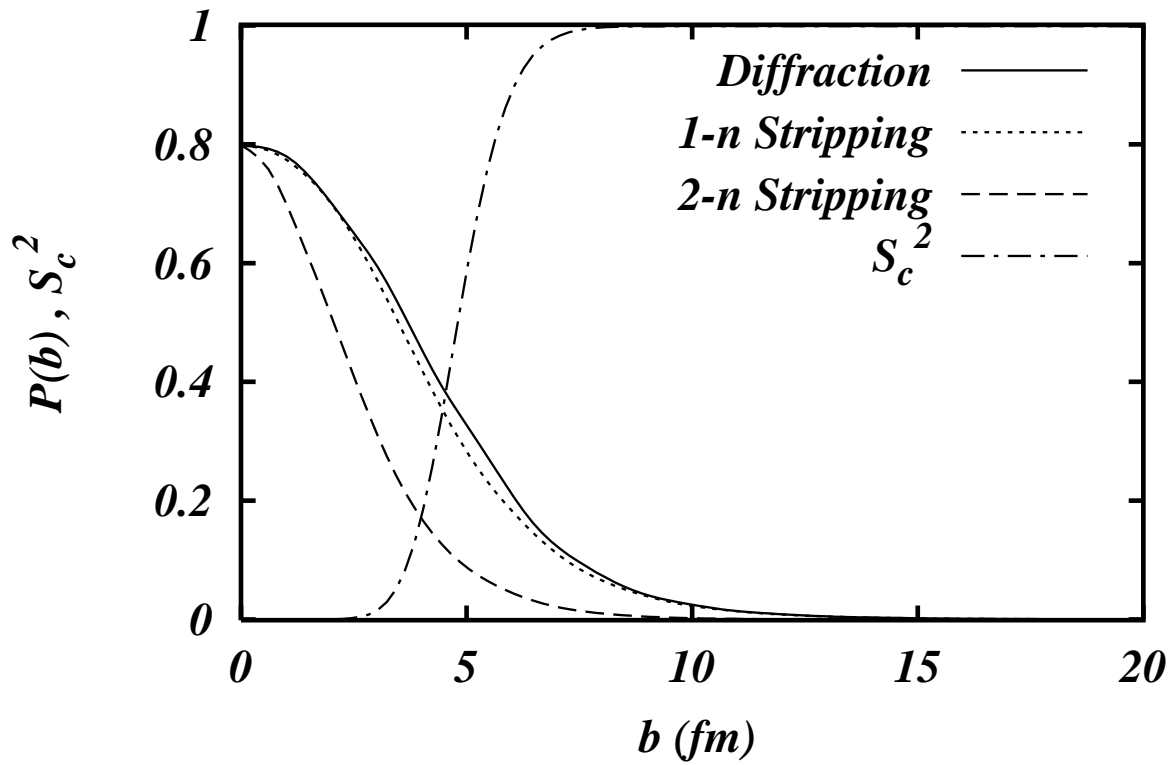


FIG. 4. Impact parameter dependence of the 1n- and 2n-stripping and the diffractive cross sections. Also shown is the square of the profile function of the core-target interaction,  $S_c^2$ .

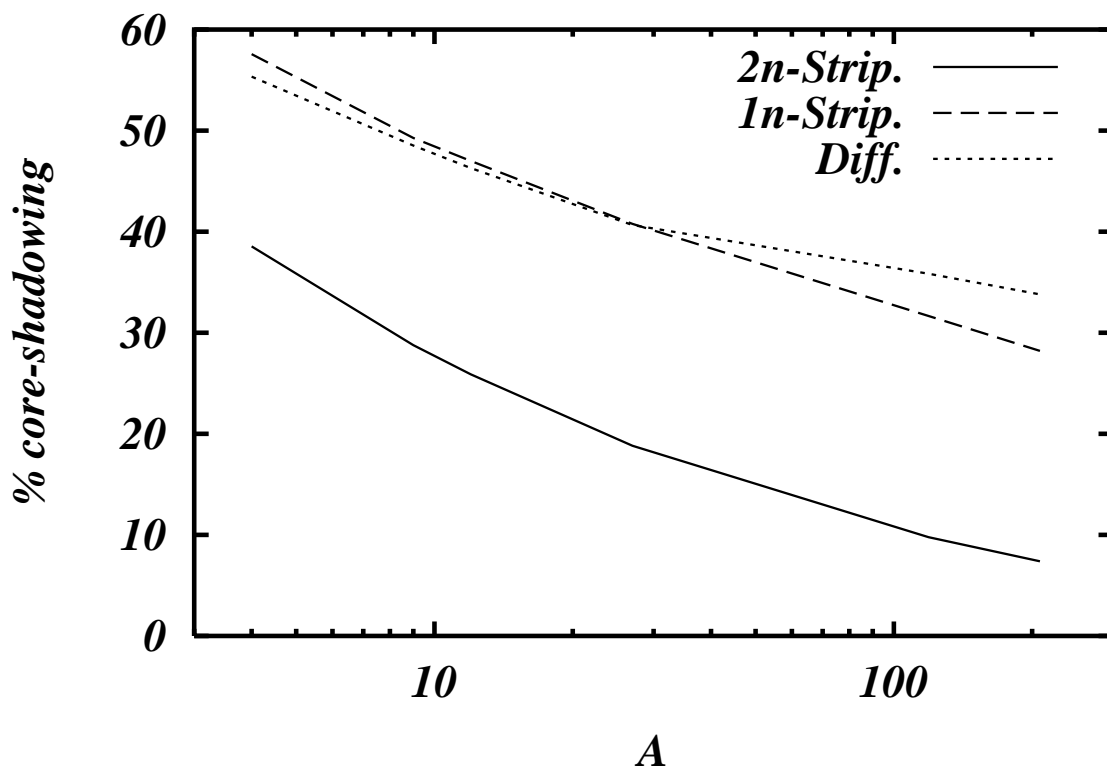


FIG. 5. Shadowing factor as a function of target mass number. Shadowing factors are shown for 2n-stripping, 1n-stripping, and diffractive cross sections at an energy of 280 MeV/n.

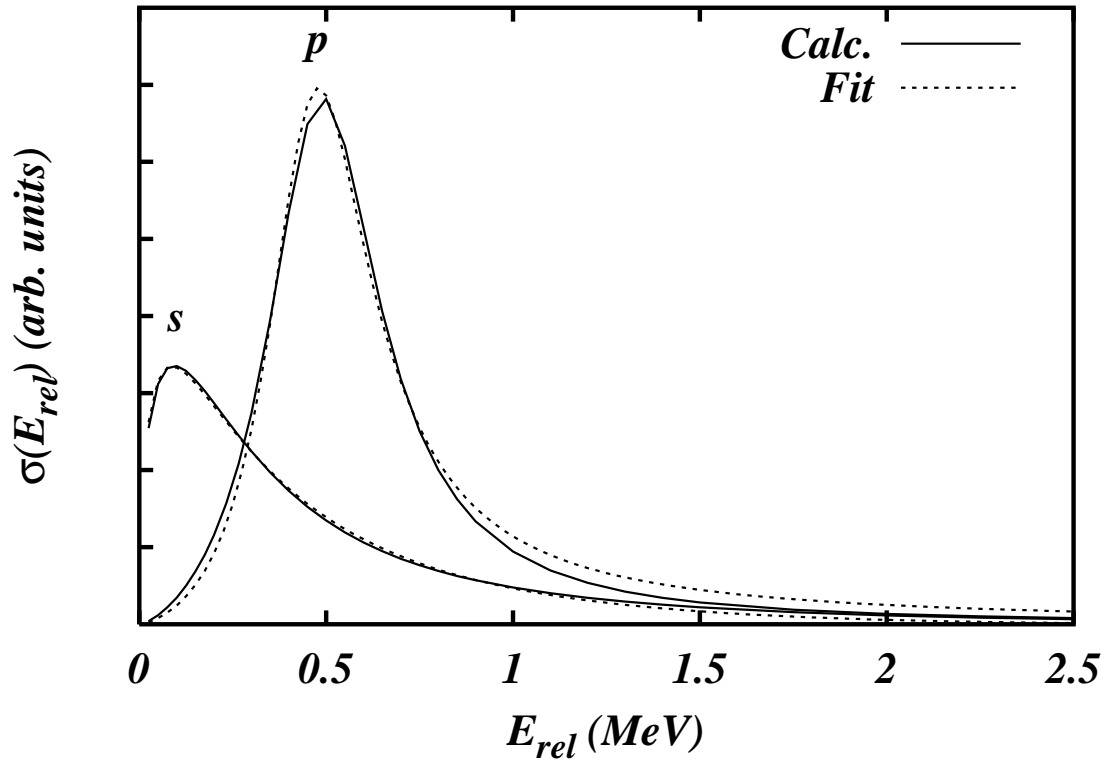


FIG. 6. The  $^{11}\text{Li}$  1n-stripping energy distributions in the no-recoil, transparent limit (solid curves) are compared to fits obtained from eq. (20) and eqs. (21,22) (dashed curves). Shown are the  $s$ - and  $p$ -wave components of the  $s_{23}$  wave function.

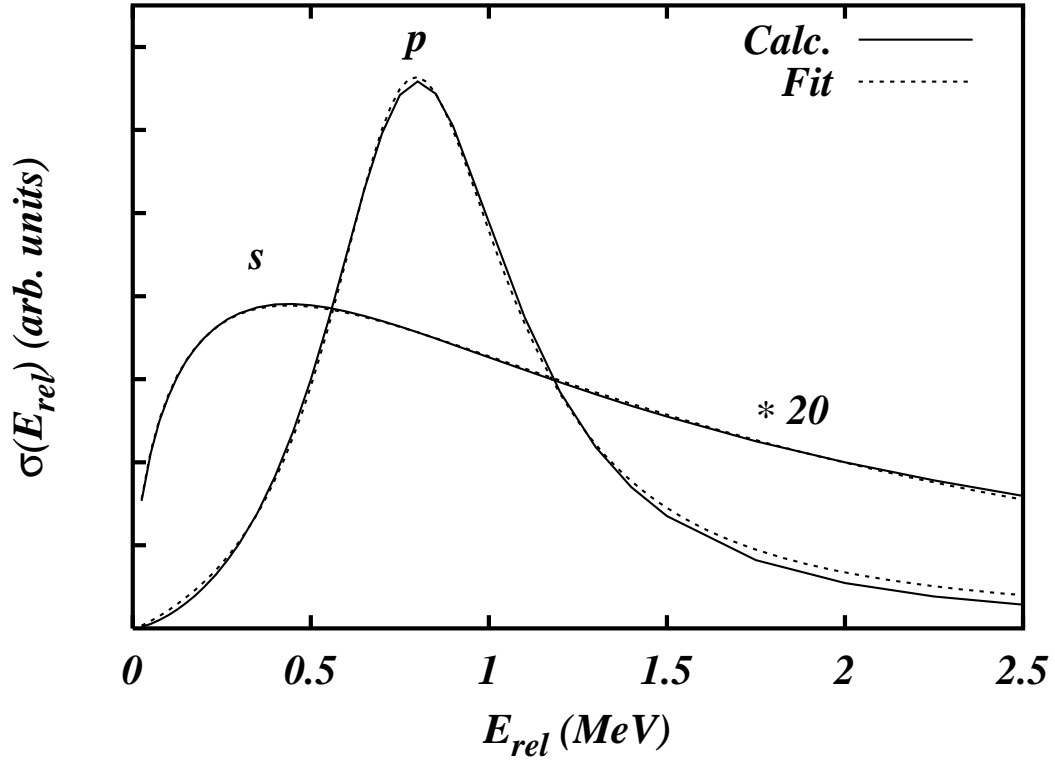


FIG. 7. The  ${}^6\text{He}$  1n-stripping energy distributions calculated in the no-recoil, transparent limit (solid curves) are compared to fits obtained from eq. (20) and eqs. (21,22) (dashed curves). The  $s$ -wave components has been scaled by a factor of 20.

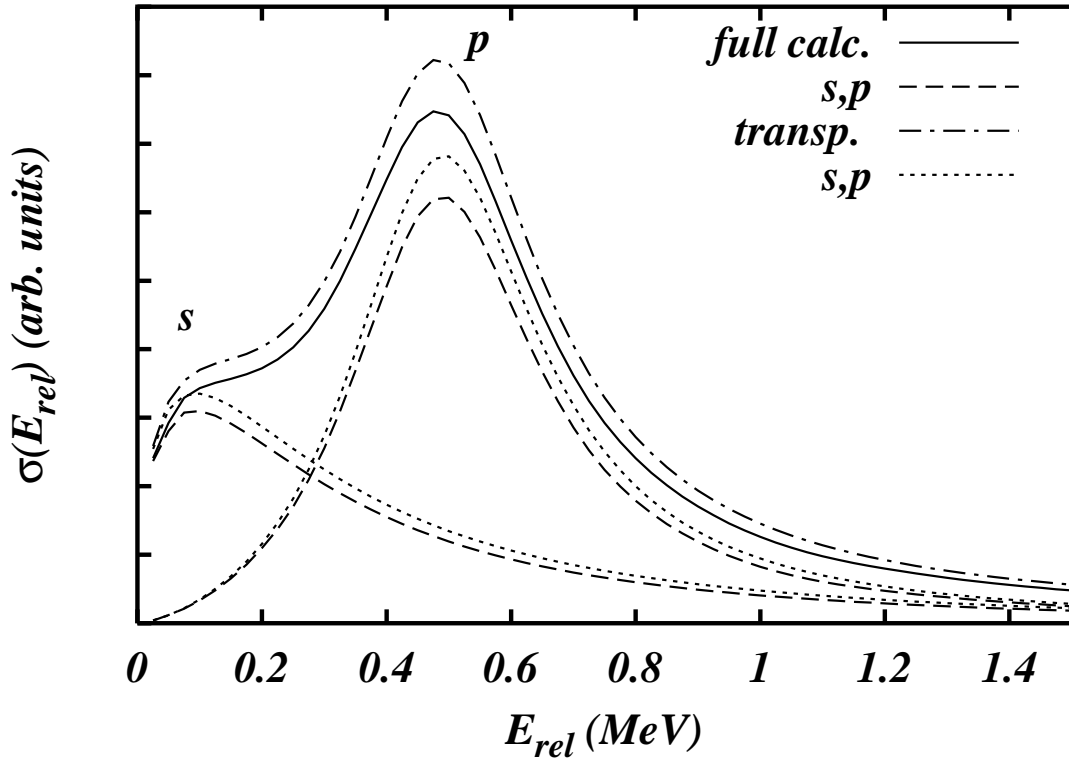


FIG. 8. Comparison of the full calculation (including shadowing of the spectator neutron) with the transparent limit. Shown are the total 1n-stripping energy distribution as well as the  $s$ - and  $p$ -wave components of the s23 model.

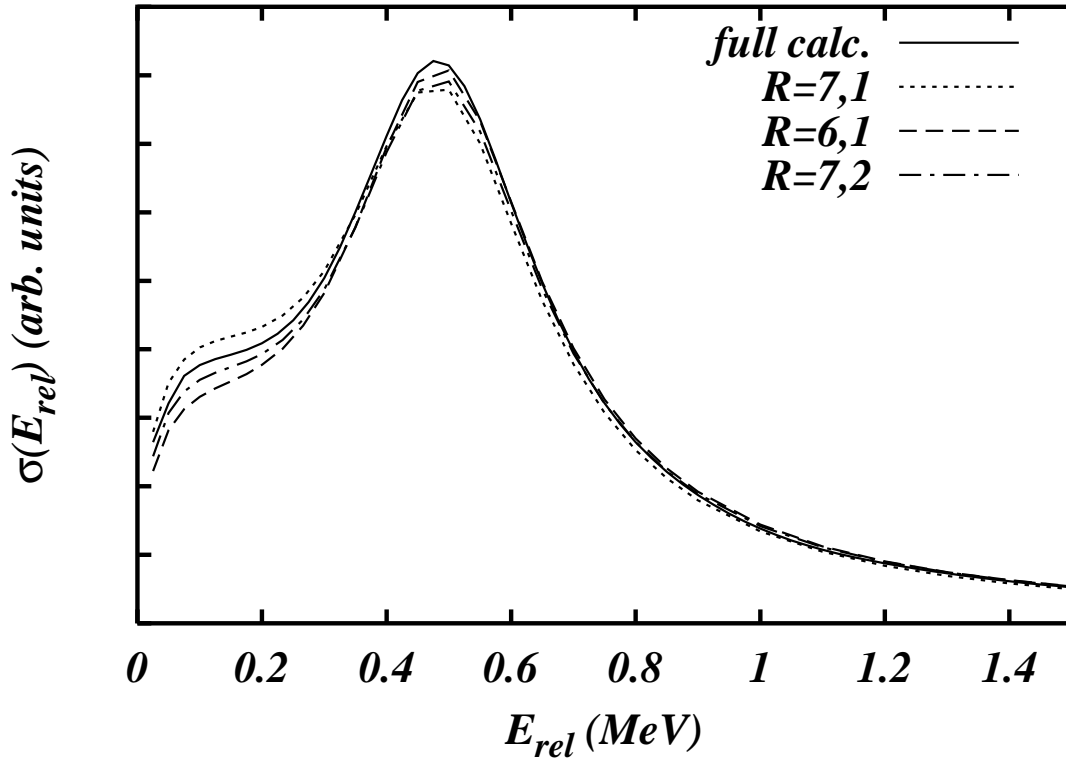


FIG. 9. Comparison of the 1n-stripping energy distribution of  $^{11}\text{Li}$  with calculations with fixed impact parameters of the nucleon-core system (6 and 7fm) and the stripped neutron (1 and 2 fm). The different spectra have been normalized to the same total value.

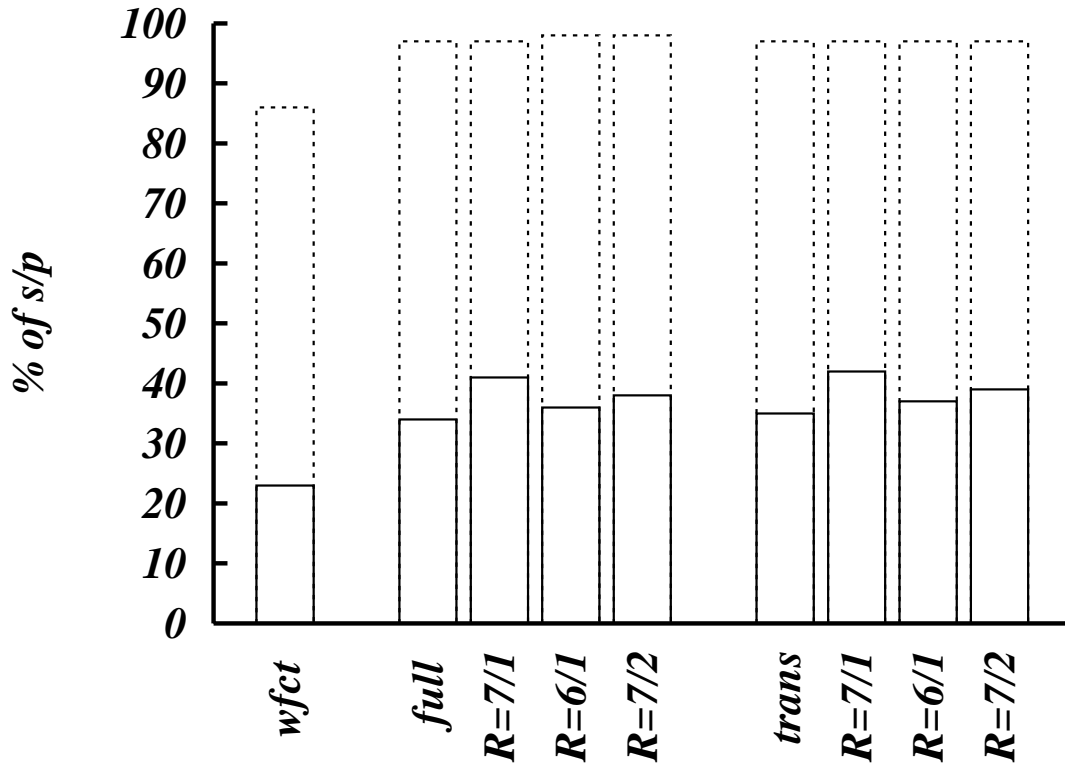


FIG. 10. Percentage of  $s$ - and  $p$ -wave in the  $s_{23}$  wave function (*wfct*), compared to the percentages remaining in the neutron-core final state following  $1n$ -stripping. The different histograms show the results of the full calculation and the transparent limit integrated over all impact parameters as well as at specific fixed values of the impact parameter of the nucleon-core system (6 and 7 fm) and the stripped neutron (1 and 2 fm).

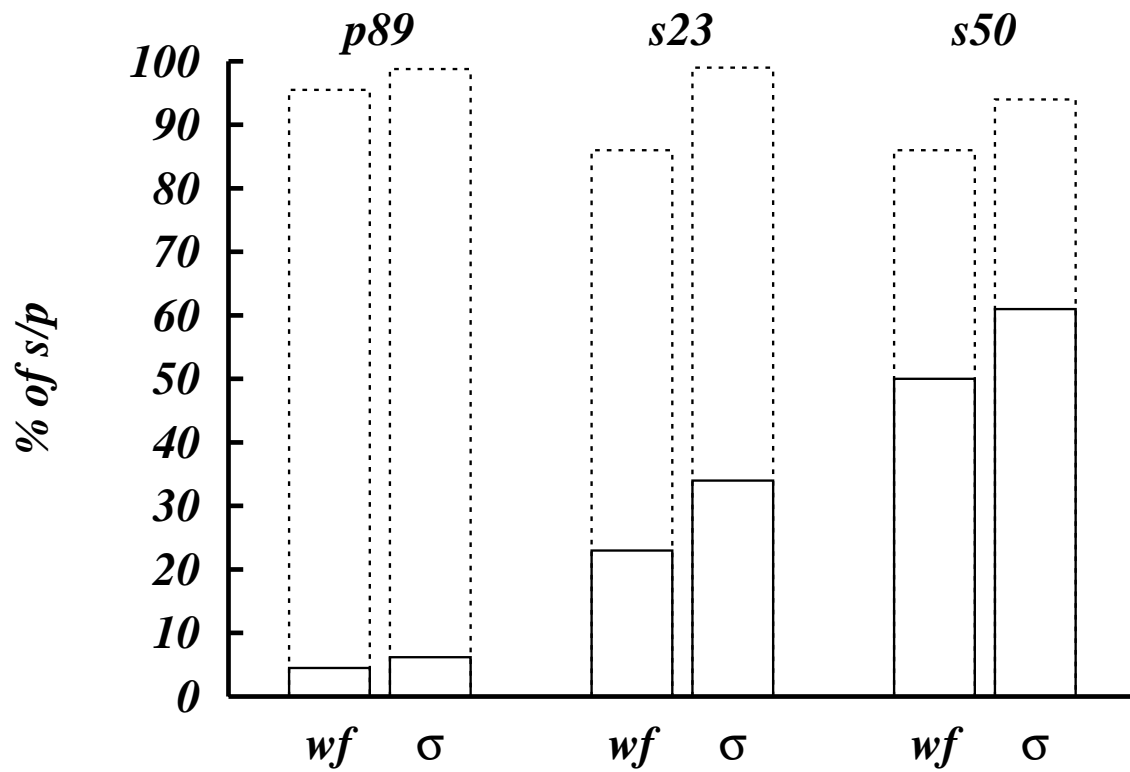


FIG. 11. Percentage of *s*- and *p*-wave in the various models, comparing the probabilities in the wave functions (*wf*) to the probabilities in the neutron-core final states ( $\sigma$ ).

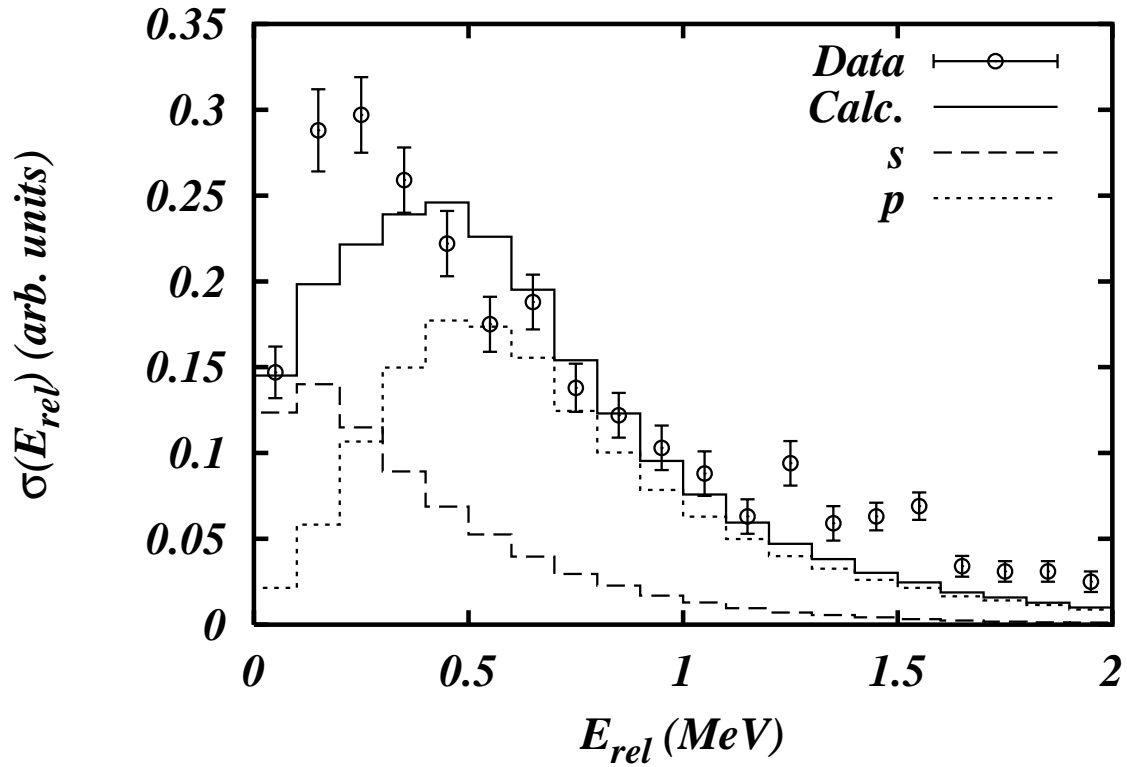


FIG. 12. Energy distribution of the s23 wave function. The histogram is the calculated result including the experimental resolution. The solid line is the result for all partial waves. Also shown are the  $s$ - and  $p$ -wave components (dashed and dotted lines). The data points are from ref. [6].

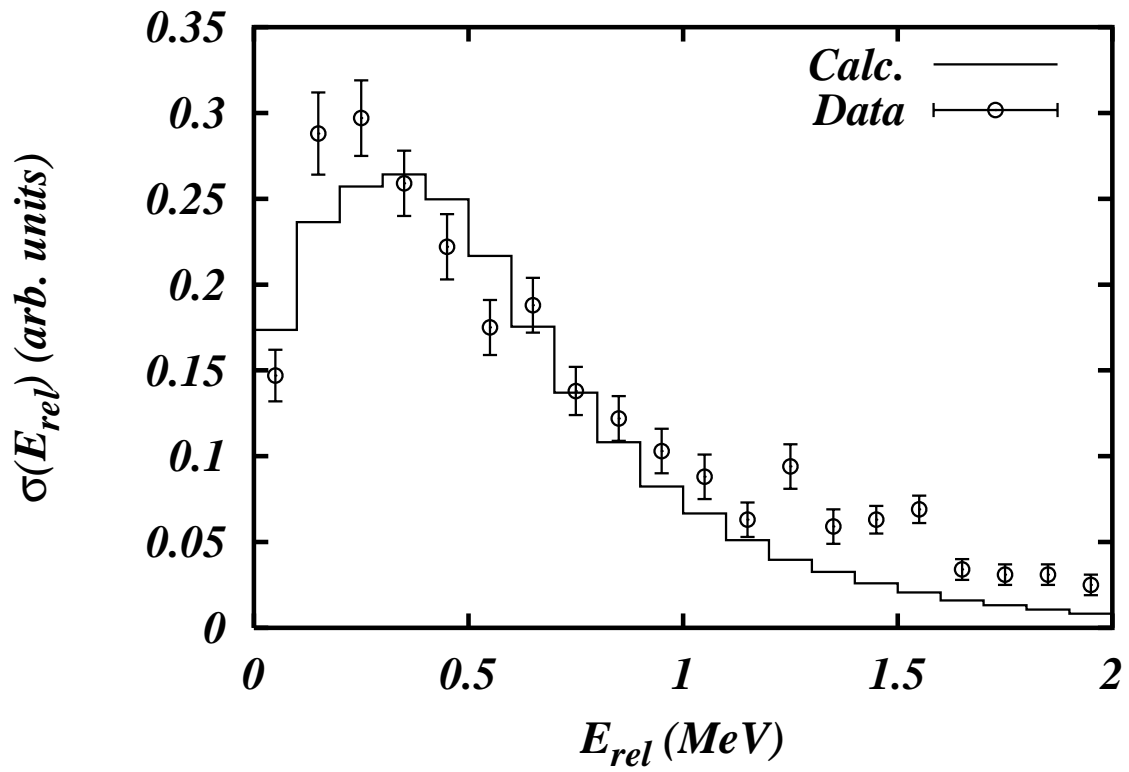


FIG. 13. “Best” fit of the energy distribution compared to the data of ref. [6]. The ratio of  $s$ - and  $p$ -wave and also the position of the  $p$ -wave resonance was varied.

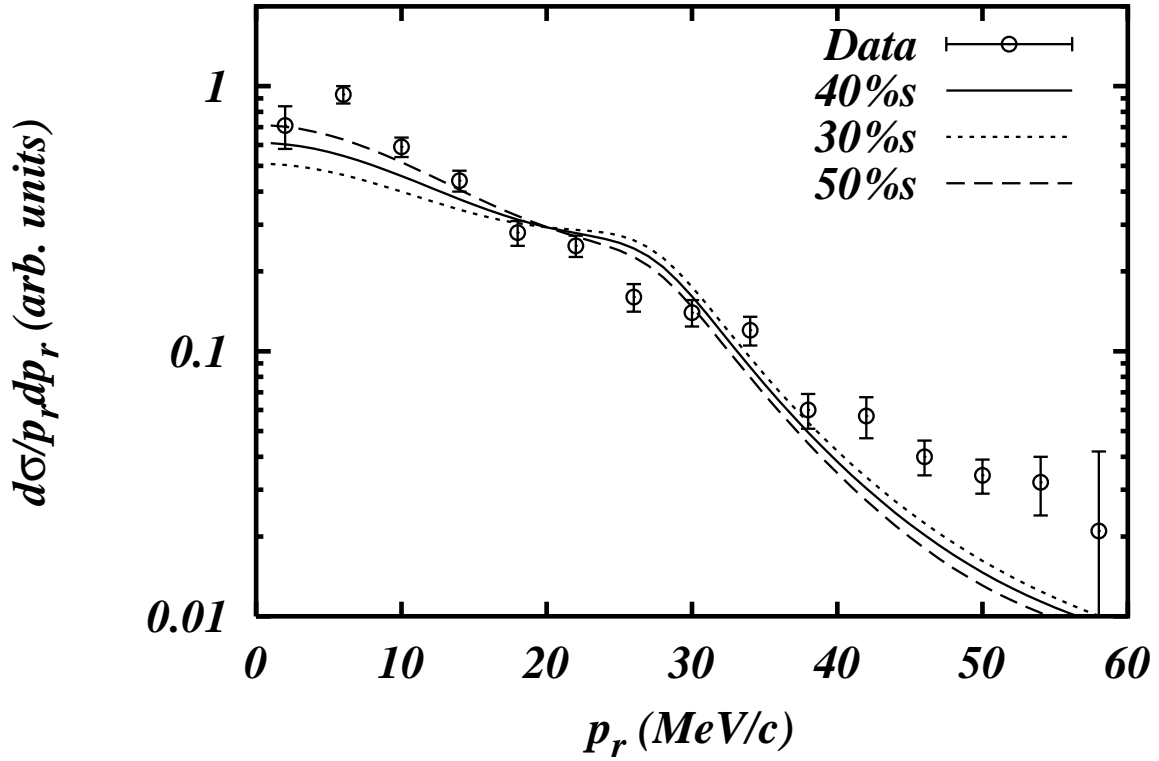


FIG. 14. Transverse momentum distribution including all partial waves of the best fit model. Shown are the results with 30,40, and 50% s-wave component in the final state, corresponding to a  $^{11}\text{Li}$ -ground state component between 20 and 40 %. The data points are from ref. [32].